



HAL
open science

TransCom N₂O model inter-comparison – Part 2: Atmospheric inversion estimates of N₂O emissions

R. Thompson, K. Ishijima, E. Saikawa, M. Corazza, U. Karstens, P. Patra, P. Bergamaschi, F. Chevallier, E. Dlugokencky, R. Prinn, et al.

► **To cite this version:**

R. Thompson, K. Ishijima, E. Saikawa, M. Corazza, U. Karstens, et al.. TransCom N₂O model inter-comparison – Part 2: Atmospheric inversion estimates of N₂O emissions. *Atmospheric Chemistry and Physics*, 2014, 14 (12), pp.6177-6194. 10.5194/ACP-14-6177-2014 . hal-02950744

HAL Id: hal-02950744

<https://hal.science/hal-02950744>

Submitted on 8 Oct 2020

HAL is a multi-disciplinary open access archive for the deposit and dissemination of scientific research documents, whether they are published or not. The documents may come from teaching and research institutions in France or abroad, or from public or private research centers.

L'archive ouverte pluridisciplinaire **HAL**, est destinée au dépôt et à la diffusion de documents scientifiques de niveau recherche, publiés ou non, émanant des établissements d'enseignement et de recherche français ou étrangers, des laboratoires publics ou privés.



TransCom N₂O model inter-comparison – Part 2: Atmospheric inversion estimates of N₂O emissions

R. L. Thompson^{1,2}, K. Ishijima³, E. Saikawa^{4,5}, M. Corazza⁶, U. Karstens⁷, P. K. Patra³, P. Bergamaschi⁶,
F. Chevallier², E. Dlugokencky⁸, R. G. Prinn⁴, R. F. Weiss⁹, S. O'Doherty¹⁰, P. J. Fraser¹¹, L. P. Steele¹¹,
P. B. Krummel¹¹, A. Vermeulen¹², Y. Tohjima¹³, A. Jordan⁷, L. Haszpra^{14,15}, M. Steinbacher¹⁶, S. Van der Laan^{17,*},
T. Aalto¹⁸, F. Meinhardt¹⁹, M. E. Popa^{7,20}, J. Moncrieff²¹, and P. Bousquet²

¹Norwegian Institute for Air Research, Kjeller, Norway

²Laboratoire des Sciences du Climat et l'Environnement, Gif sur Yvette, France

³Research Institute for Global Change, JAMSTEC, Yokohama, Japan

⁴Center for Global Change Science, MIT, Cambridge, MA, USA

⁵Emory University, Atlanta, GA, USA

⁶Institute for Environment and Sustainability, JRC, Ispra, Italy

⁷Max Planck Institute for Biogeochemistry, Jena, Germany

⁸NOAA Earth System Research Laboratory, Global Monitoring Division, Boulder, CO, USA

⁹Scripps Institution of Oceanography, La Jolla, CA, USA

¹⁰Atmospheric Chemistry Research Group, School of Chemistry, University of Bristol, Bristol, UK

¹¹Centre for Australian Weather and Climate Research, CSIRO, Marine and Atmospheric Research, Aspendale, Victoria, Australia

¹²Energy Research Centre of the Netherlands (ECN), Petten, the Netherlands

¹³National Institute for Environmental Studies, Tsukuba, Japan

¹⁴Hungarian Meteorological Service, Budapest, Hungary

¹⁵Geodetic and Geophysical Institute, Research Centre for Astronomy and Earth Sciences, Hungarian Academy of Sciences, Sopron, Hungary

¹⁶Swiss Federal Laboratories for Materials Science and Technology (Empa), Dübendorf, Switzerland

¹⁷Institute for Marine and Atmospheric Research Utrecht, University of Utrecht, Utrecht, the Netherlands

¹⁸Finnish Meteorological Institute, Helsinki, Finland

¹⁹Umweltbundesamt, Messstelle Schauinsland, Kirchzarten, Germany

²⁰Centre for Isotope Research, University of Groningen, Groningen, the Netherlands

²¹School of GeoSciences, The University of Edinburgh, Edinburgh, UK

* now at: School of Environmental Sciences, University of East Anglia, Norwich, UK

Correspondence to: R. L. Thompson (rona.thompson@nilu.no)

Received: 15 November 2013 – Published in Atmos. Chem. Phys. Discuss.: 27 February 2014

Revised: 9 May 2014 – Accepted: 16 May 2014 – Published: 23 June 2014

Abstract. This study examines N₂O emission estimates from five different atmospheric inversion frameworks based on chemistry transport models (CTMs). The five frameworks differ in the choice of CTM, meteorological data, prior uncertainties and inversion method but use the same prior emissions and observation data set. The posterior modelled atmospheric N₂O mole fractions are compared to observations to

assess the performance of the inversions and to help diagnose problems in the modelled transport. Additionally, the mean emissions for 2006 to 2008 are compared in terms of the spatial distribution and seasonality. Overall, there is a good agreement among the inversions for the mean global total emission, which ranges from 16.1 to 18.7 TgN yr⁻¹ and is consistent with previous estimates. Ocean emissions

represent between 31 and 38 % of the global total compared to widely varying previous estimates of 24 to 38 %. Emissions from the northern mid- to high latitudes are likely to be more important, with a consistent shift in emissions from the tropics and subtropics to the mid- to high latitudes in the Northern Hemisphere; the emission ratio for 0–30° N to 30–90° N ranges from 1.5 to 1.9 compared with 2.9 to 3.0 in previous estimates. The largest discrepancies across inversions are seen for the regions of South and East Asia and for tropical and South America owing to the poor observational constraint for these areas and to considerable differences in the modelled transport, especially inter-hemispheric exchange rates and tropical convective mixing. Estimates of the seasonal cycle in N₂O emissions are also sensitive to errors in modelled stratosphere-to-troposphere transport in the tropics and southern extratropics. Overall, the results show a convergence in the global and regional emissions compared to previous independent studies.

1 Introduction

Nitrous oxide (N₂O) currently has the third largest contribution to net radiative forcing after CO₂ and CH₄, and currently has radiative forcing of 0.17 Wm⁻² (Myhre et al., 2013). Furthermore, N₂O plays an important role in stratospheric ozone loss and currently the ozone-depleting-potential weighted emissions of N₂O are thought to be the highest of any ozone-depleting substance (Ravishankara et al., 2009). The atmospheric mole fraction of N₂O has increased significantly since the mid-20th century largely as a result of agricultural activities and, in particular, the use of nitrogen fertilizers (Park et al., 2012). Currently, agricultural emissions from fertilizer use and manure management (4.3–5.8 TgN yr⁻¹) and emissions from natural soils (6–7 TgN yr⁻¹) account for 60–70 % of global N₂O emissions (Syakila and Kroeze, 2011; Zaehle et al., 2011). The remaining 30–40 % of emissions is from oceans (4.5 TgN yr⁻¹) (Duce et al., 2008) and, to a smaller extent, from fuel combustion, industry (Olivier et al., 2005) and biomass burning (together 1.7 TgN yr⁻¹) (van der Werf et al., 2010).

N₂O is dominantly produced by microbial processes in soils, sediments and water bodies – specifically, by nitrification and denitrification. Although a lot is already known about these processes from laboratory studies under controlled conditions and in situ chamber flux measurements, upscaling to emissions on national or regional scales is hampered by the strongly variable nature of soil fluxes. N₂O production in soils is dependent on a multitude of environmental factors such as soil moisture and temperature, soil type, among others, which interact in complex ways and are difficult to predict. In agricultural soils, the type of nitrogen fertilizer and the timing of its application are also important considerations for estimating N₂O emissions. In natural soils,

there is a natural nitrogen turnover leading to N₂O emissions but these may be enhanced by the input of reactive nitrogen from fertilizers and other anthropogenic sources by atmospheric transport, erosion and leaching, leading to so-called indirect anthropogenic emissions (Galloway et al., 2003).

An alternative and complementary approach to upscaling small-scale fluxes and processes to estimate regional and global N₂O budgets, is to use a top-down approach. Atmospheric inversion is one such top-down approach and uses observations of N₂O mole fractions with a model of atmospheric transport and chemistry in a statistically rigorous way to constrain surface fluxes. This approach has been used previously for estimating N₂O emissions on regional (Corazza et al., 2011; Thompson et al., 2011b) and global scales (Hirsch et al., 2006; Huang et al., 2008; Kort et al., 2011; Prinn et al., 1990; Saikawa et al., 2014; Thompson et al., 2014a). One major advantage of the atmospheric inversion approach is that it provides a constraint on the total N₂O emission since the atmosphere integrates the fluxes and requires that the change in atmospheric N₂O abundance be balanced by the sum of its sources and sinks. In general terms, upscaling approaches provide a detailed picture of the processes and source types while top-down approaches provide an integrated picture of the regional and long-term emissions and a check on the total budget. However, atmospheric inversions also have sources of error. The estimated fluxes are sensitive to errors in the modelled transport and, to varying degrees, the chemistry, as these are non-random errors that are extremely difficult to estimate and account for in an inversion framework. Particularly for N₂O, errors in stratosphere–troposphere exchange (STE) represent an important source of model error since there is a strong N₂O mole fraction gradient across the tropopause owing to the loss of N₂O through photolysis and reaction with O(¹D) in the stratosphere (see Part 1, Thompson et al., 2014b).

Part 1 of the TransCom N₂O experiment examined the importance of atmospheric transport and surface fluxes on tropospheric N₂O mole fractions and, specifically, looked at the influence of transport model errors on N₂O mole fractions on seasonal to annual timescales (Thompson et al., 2014b). In this paper (Part 2), we present N₂O emission estimates from five inversion frameworks based on five different atmospheric chemistry transport models (CTMs), all of which also participated in Part 1. In this context, the objectives of this paper are to:

- compare the posterior emissions (i.e. resulting from the inversions) in a standardized way
- analyse the posterior emissions in terms of spatial distribution, seasonal variability, and to identify robust features common to all inversions
- identify regions where there are discrepancies between inversions and investigate their cause

Table 1. Overview of the CTMs used in the inversions. Note that the horizontal resolution is given as longitude by latitude.

| Model | Institute | Resolution | | Top boundary pressure (hPa) | Meteorology |
|------------|-----------|--------------|--------------------------|-----------------------------|-------------|
| | | horizontal | vertical | | |
| MOZART4 | MIT | 2.5° × 1.88° | 56 σ ¹ | 2 | MERRA |
| ACTMt42l67 | JAMSTEC | 2.8° × 2.8° | 67 σ | 0.01 | JRA25 |
| TM3 | MPI-BGC | 5.0° × 3.75° | 26 η ² | 1 | ERA-Interim |
| TM5 | JRC | 6.0° × 4.0° | 25 η | 0.5 | ERA-Interim |
| LMDZ4 | LSCE | 3.75° × 2.5° | 19 η | 4 | ERA-Interim |

¹ σ refers to the sigma terrain-following vertical coordinate system.

² η refers to the eta coordinate system that smoothly transitions from the sigma coordinate near the surface to a pressure coordinate in the stratosphere.

- present regional emissions estimates and their uncertainties

This paper is divided into four main sections. In Sect. 2, we outline the inversion frameworks and CTMs, as well as the prior flux estimates and atmospheric observations used in this study. Section 3.1 presents a validation of the inversion results by comparing the mole fractions simulated using the posterior fluxes with observations, while Sect. 3.2 analyses the spatial and temporal distribution of the posterior fluxes. In Sect. 3.3, we compare these estimates with those of previous studies and conclude with a discussion of the major challenges for estimating N₂O emissions from atmospheric inversions.

2 Methods

2.1 Inversion frameworks

Five different inversion frameworks participated in Part 2 of this experiment. In this paper, we refer to each of the frameworks according to the CTM used followed by “-I” to indicate that this is the inversion framework. Although the frameworks may be used with a different CTM, in this study the naming is unambiguous as a different CTM was used with each one (see Table 1). All frameworks use the Bayesian inversion method to find the optimal surface fluxes, that is, the fluxes that provide the best fit to the atmospheric observations, \mathbf{y} , while being guided by the prior flux estimates, \mathbf{x}_b , and their uncertainties (for details about the Bayesian method refer to Tarantola, 2005). Based on Bayesian theory, and Gaussian-error hypotheses, the optimal fluxes are those that minimize the cost function

$$J(\mathbf{x}) = (\mathbf{x} - \mathbf{x}_b)^T \mathbf{B}^{-1} (\mathbf{x} - \mathbf{x}_b) + (H(\mathbf{x}) - \mathbf{y})^T \mathbf{R}^{-1} (H(\mathbf{x}) - \mathbf{y}), \quad (1)$$

where the prior flux uncertainties are described by the error covariance matrix, \mathbf{B} , the observation uncertainties are described by the error covariance matrix, \mathbf{R} , and H is an operator of the atmospheric transport and chemistry as defined

by the CTM in each inversion framework. Depending on the inversion framework, H is either a matrix or a non-linear operator. The frameworks differ in how the minimum of the cost function (Eq. 1) is sought. Approaches for finding the \mathbf{x} that minimizes this equation fall into one of the following categories: (1) variational methods, such as those used in weather forecasting (Courtier et al., 1994) and (2) analytical methods (Tarantola, 2005). Variational methods find the optimal \mathbf{x} using an iterative descent algorithm, usually requiring calculation of the gradient of J at each iteration, and do not require H to be a matrix operator (Chevallier et al., 2005). Analytical methods require that the transport operator H is linear and defined (i.e. \mathbf{H}) and the optimal (posterior) \mathbf{x} is found by solving Eq. (2) or (3) directly (for a derivation of these equations refer to Tarantola, 2005):

$$\mathbf{x} = \mathbf{x}_b + (\mathbf{H}^T \mathbf{R}^{-1} \mathbf{H} + \mathbf{B}^{-1})^{-1} \mathbf{H}^T \mathbf{R}^{-1} (\mathbf{y} - \mathbf{H} \mathbf{x}_b) \quad (2)$$

$$\mathbf{x} = \mathbf{x}_b + \mathbf{B} \mathbf{H}^T (\mathbf{H} \mathbf{B} \mathbf{H}^T + \mathbf{R})^{-1} (\mathbf{y} - \mathbf{H} \mathbf{x}_b) \quad (3)$$

(analytical methods can also be used in the case that H is non-linear if it is still differentiable and that the linear \mathbf{H} can be defined over a small range of \mathbf{x} , in which case, an outer loop is also required to better approximate \mathbf{H}). For inversions falling into the first category, an adjoint model of the atmospheric chemistry and transport is used to calculate the gradient and to find the minimum; the TM5-I, TM3-I, and LMDZ4-I frameworks fall into this category (see Table 2). For inversions in the second category, the chemistry-transport operator, \mathbf{H} , represents the sensitivity of the observations to the fluxes in each of a given number of predefined regions. Each column of \mathbf{H} can be found by running the CTM, perturbing the fluxes in a given region, and determining the resulting change atmospheric mole fraction for all observations. The emissions sensitivity is thus the ratio of the change in mole fraction to the change in flux; the ACTMt42l67-I and MOZART4-I frameworks fall into this category (see Table 2).

Table 2. Overview of the inversion frameworks. The matrix **B** is the prior flux error covariance matrix (see Eq. 1).

| Model | Resolution | | Inversion method | Scale length in B (km) | |
|---------------------------|-------------------------|----------|------------------|-------------------------------|-------|
| | Spatial | Temporal | | Land | Ocean |
| MOZART4-I ¹ | 13 regions | monthly | Analytical | none | none |
| ACTMt42167-I ² | 22 regions ⁶ | monthly | Analytical | none | none |
| TM3-I ³ | 5.0° × 3.75° | monthly | Variational | 500 | 500 |
| TM5-I ⁴ | 6.0° × 4.0° | monthly | Variational | 200 | 200 |
| LMDZ4-I ⁵ | 3.75° × 2.5° | monthly | Variational | 500 | 1000 |

¹ Saikawa et al. (2013), ² based on Rayner et al. (1999), ³ Rödenbeck (2005), ⁴ Corazza et al. (2011), ⁵ Thompson et al. (2011a), ⁶ TransCom-3 regions.

Table 3. Prior flux model overview (totals shown for 2005).

| Category | Data set | Resolution | Total (TgN yr ⁻¹) |
|----------------------------------|---------------|------------|-------------------------------|
| Terrestrial biosphere | ORCHIDEE O-CN | monthly | 10.83 |
| Ocean | PISCES | monthly | 4.28 |
| Waste water | EDGAR-4.1 | annual | 0.21 |
| Solid waste | EDGAR-4.1 | annual | 0.004 |
| Solvents | EDGAR-4.1 | annual | 0.05 |
| Fuel production | EDGAR-4.1 | annual | 0.003 |
| Ground transport | EDGAR-4.1 | annual | 0.18 |
| Industry combustion | EDGAR-4.1 | annual | 0.41 |
| Residential and other combustion | EDGAR-4.1 | annual | 0.18 |
| Shipping | EDGAR-4.1 | annual | 0.002 |
| Other sources | EDGAR-4.1 | annual | 0.0005 |
| Biomass burning | GFED-2 | monthly | 0.71 |
| Total | | monthly | 16.84 |

2.2 Experiment protocol

As in Part 1, all participants were requested to use the same atmospheric observations, prior flux estimates and approximate magnitude of the stratospheric sink. Thereby, the sources of differences between inversion results are limited to the choice of CTM and meteorological data, the inversion method, and uncertainties assigned to the prior fluxes and the observations. Furthermore, since the CTMs used in each of the inversion frameworks are the same as those used in Part 1, the analysis of the transport model performance can be directly applied in this study when considering differences between posterior fluxes. All inversions were run for the period 2005–2009 but only output from 2006 onwards was analysed as 2005 was used as a spin-up year. A spin-up period is required to minimize the influence of the initial conditions on the posterior emissions. Here, we chose 1 year for the spin-up as all models started with their best initial conditions estimates established after previous longer integrations of the CTMs. Also, when presenting mean emission results, the years 2006–2008 are used, as the end of 2009 is not as well constrained in the inversions (to constrain the end of 2009, observations at the beginning of 2010 would need

to be included and these were not all available at the time of preparing this study).

2.2.1 Stratospheric N₂O loss

Loss of N₂O in the stratosphere through photolysis (circa 90 % of the loss; Minschwaner et al., 1993) and reaction with O(¹D) (circa 10 %) was calculated in each model in every grid cell and time step. Although the exact photolysis and oxidation rates varied between models (according to the CTM used to calculate the photolysis rate and O(¹D) concentration) these were scaled such that the global annual total loss of N₂O was approximately 12.5 TgN, consistent with estimates of the atmospheric abundance and the lifetime of N₂O, which is estimated to be between 124 and 130 years (Prather et al., 2012; Volk et al., 1997).

2.2.2 Prior fluxes

The prior N₂O flux was comprised from estimates of the different sources, that is, from soils (including both natural and agricultural soils), ocean, biomass burning, waste, fuel combustion and industry (see Table 3). For soil fluxes, we used the terrestrial biosphere model, O-CN (Zaehle and Friend, 2010), which is driven by reconstructed observed climate

(CRU-NCEP, Climate Research Unit–National Centre for Environmental Prediction), N-fertilizer application, and atmospheric N-deposition data and provides inter-annually varying estimates at monthly and $3.75^\circ \times 2.5^\circ$ (longitude by latitude) resolution as described in Zaehle et al. (2011). For the ocean flux, we used the Pelagic Interaction Scheme for Carbon and Ecosystem Studies (PISCES) ocean biogeochemistry model (Dutreuil et al., 2009), which provides inter-annually varying fluxes at monthly and $1.0^\circ \times 1.0^\circ$ resolution. For waste, fuel combustion and industrial emissions, we used EDGAR-4.1 (Emission Database for Greenhouse gas and Atmospheric Research, available at: <http://edgar.jrc.ec.europa.eu/index.php>), which are estimated for the reference year 2005 and were provided annually at $1.0^\circ \times 1.0^\circ$ resolution. Biomass burning estimates from GFED-2.1 (Global Fire Emissions Database) (van der Werf et al., 2010) were used, which were provided monthly and at $1.0^\circ \times 1.0^\circ$ resolution. In total, the global emission for 2005 to 2009 was 16.8, 16.3, 16.8, 16.2 and 16.4 TgN yr⁻¹, respectively.

2.2.3 Uncertainty estimates

The prior flux uncertainties were determined following the method usually used for the respective frameworks. For TM5-I, the uncertainties were calculated for each grid cell as 100 % of the annual mean prior value. For LMDZ4-I, the uncertainties were chosen for each grid cell as 100 % of the maximum of the eight surrounding grid cells plus the one of interest. These were used to form the variances and the square root of total of the prior error covariance matrix was scaled to be equal to 2 TgN yr⁻¹. For TM3-I the uncertainties of the prior flux were calculated as 100 % of the flux per grid cell and month. Lastly, for ACTMt42167-I and MOZART4-I, the regional uncertainty was chosen to be 100 and 50 %, respectively, of the regional emission.

Similarly, each inversion framework has a different estimation method for the representation uncertainty, that is, the uncertainty due to the modelled transport and the temporal representation uncertainty. The transport uncertainties are calculated as follows: TM5-I and LMDZ4-I use the method of Bergamaschi et al., 2010; TM3-I uses pre-determined values for the uncertainty at marine (1.6 ppb), mountain (2.4 ppb), continental (4.8 ppb), and coastal (2.4 ppb) locations; MOZART4-I uses the gradient of the monthly mean mixing ratio between the grid cell where the observation site is located and the eight surrounding grid cells; and ACTMt42167 uses the 3-D gradient (using the four horizontal and two vertical grid cells) surrounding the observation site. The temporal representation uncertainties are calculated as follows: TM5-I and LMDZ4-I assimilate afternoon/night-time mean mixing ratios for low-altitude/mountain sites, respectively, and use the standard deviation of the afternoon/night mean mixing ratio at each site; MOZART4-I assimilates the monthly mean mixing ratio and uses the standard error of the monthly mixing ratio at each site;

ACTMt42167 also assimilates the monthly mean mixing ratio and uses the standard error of the monthly mixing ratio multiplied by a factor of 2 to account for the underestimation of the variability in the model; and TM3-I assimilates the weekly mean mixing ratio but does not include an estimate of the temporal representation uncertainty.

2.2.4 Degrees of freedom

The number of degrees of freedom in the inversion is an important factor for determining how closely the posterior fluxes resemble the prior ones. For MOZART4-I and ACTMt42167-I, which solve the inversion using coarse regions, the number of degrees of freedom is substantially reduced, representing a strong constraint on the inversion as only the mean flux in each region is optimized and the flux pattern within each region remains as described a priori. On the other hand, solving for fine regions i.e. at the resolution of the transport model, as in TM5-I, TM3-I and LMDZ4-I, benefits from additional regularization constraints, such as spatial correlations of the prior flux errors (used in the definition of **B**). For TM5-I the spatial correlation length (200 km) means that the grid cells are only weakly correlated to one another resulting in a weak constraint, whereas in LMDZ4-I, longer scale lengths are used (500 km for land and 1000 km for ocean) resulting in a stronger constraint (see Table 2).

2.3 Atmospheric observations

Atmospheric observations of N₂O mole fractions (nmol mol⁻¹ equivalently parts per billion, abbreviated as ppb) were pooled from two global networks, NOAA CCGG (Carbon Cycle and Greenhouse Gases) and AGAGE (Advanced Global Atmospheric Gases Experiment), as well as from a number of smaller regional networks and independent stations (see Fig. 1 and Table 4). From the NOAA CCGG network, 42 sites were included. Approximately weekly discrete air samples are taken at these sites, which are subsequently analysed for N₂O using GC-ECD (Gas Chromatography Electron Capture Detector). These data are reported on the NOAA-2006A calibration scale (Hall et al., 2007) and have a reproducibility of 0.4 ppb based on the mean difference of flask pairs. The AGAGE network consists of five in situ GC-ECD instruments. These data are reported on the SIO-1998 scale and have a reproducibility of approximately 0.1 ppb (Prinn et al., 2000). The MPI-BGC (Max Planck Institute for Biogeochemistry) network consists of three sites for discrete air samples and two sites with in situ GC-ECD instruments. These data are also reported on the NOAA-2006A scale and have a reproducibility of about 0.3 ppb. In addition, data from nine independently run stations with in situ GC-ECD instruments were included (see Table 4).

These stations do not all use the same calibration scale and, thus, offsets exist between the measurements. Furthermore, even in the case where the measurements are reported

Table 4. Atmospheric observation sites using in the inversions. (F = Flask, C = Continuous). Altitude is specified as metres above sea level (m a.s.l.).

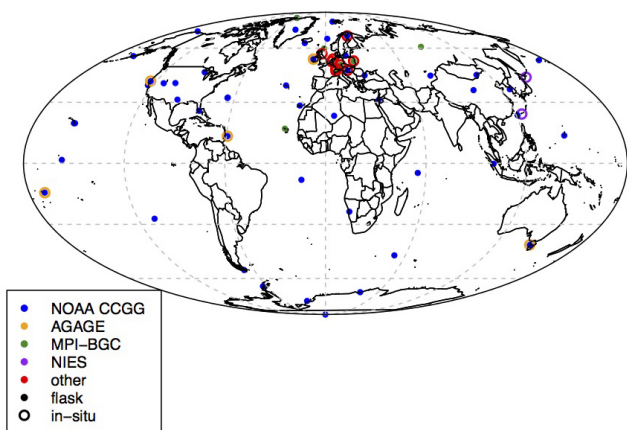
| ID | Station | Operator | Type | Latitude | Longitude | Altitude (m a.s.l.) |
|-----|-----------------------------|----------|------|----------|-----------|---------------------|
| ALT | Alert, Canada | NOAA | F | 82.5° N | 62.5° W | 210 |
| ASC | Ascension Isl., UK | NOAA | F | 7.9° S | 14.4° W | 54 |
| ASK | Assekrem, Algeria | NOAA | F | 23.2° N | 5.4° E | 2728 |
| AZR | Azores, Portugal | NOAA | F | 38.8° N | 27.4° W | 40 |
| BAL | Baltic Sea, Poland | NOAA | F | 55.4° N | 17.2° E | 7 |
| BIK | Bialystok, Poland | MPI-BGC | C | 55.3° N | 22.8° E | 460 |
| BKT | Bukit Kototabang, Indonesia | NOAA | F | 0.2° S | 100.3° E | 865 |
| BME | St. Davis Head, Bermuda, UK | NOAA | F | 32.4° N | 64.7° W | 30 |
| BMW | Tudor Hill, Bermuda, UK | NOAA | F | 32.3° N | 64.9° W | 30 |
| BRW | Barrow, Alaska | NOAA | F | 71.3° N | 156.6° W | 11 |
| BSC | Black Sea, Romania | NOAA | F | 44.2° N | 28.7° E | 3 |
| CBA | Cold Bay, Alaska | NOAA | F | 55.2° N | 162.7° W | 21 |
| CBW | Cabauw, Netherlands | ECN | C | 52.0° N | 4.9° E | 118 |
| CGO | Cape Grim, Tasmania | AGAGE | C | 40.7° S | 144.7° E | 164 |
| CHR | Christmas Isl. | NOAA | F | 1.7° N | 157.2° W | 3 |
| COI | Cape Ochi-ishi, Japan | NIES | C | 43.2° N | 145.5° E | 45 |
| CRZ | Crzot Isl., France | NOAA | F | 46.45° S | 51.9° E | 120 |
| CVR | Calhau, Cape Verde | MPI-BGC | F | 16.9° N | 24.9° W | 10 |
| EIC | Easter Island, Chile | NOAA | F | 27.2° S | 109.5° W | 50 |
| GMI | Mariana Isl., Guam | NOAA | F | 13.4° N | 144.8° E | 2 |
| HAT | Hateruma, Japan | NIES | C | 24.1° N | 123.8° E | 10 |
| HBA | Halley Stn., Antarctica | NOAA | F | 75.6° S | 26.5° W | 30 |
| HUN | Hegyhatsal, Hungary | ELTE | C | 46.9° N | 16.7° E | 344 |
| ICE | Vestmannaeyjar, Iceland | NOAA | F | 63.3° N | 20.3° W | 118 |
| IZO | Tenerife, Spain | NOAA | F | 28.3° N | 16.5° W | 2360 |
| JFJ | Jungfrauoch, Switzerland | EMPA | C | 46.6° N | 8.0° E | 3580 |
| KEY | Key Biscayne, Florida | NOAA | F | 25.7° N | 80.2° W | 3 |
| KUM | Cape Kumukahi | NOAA | F | 19.5° N | 154.8° W | 3 |
| KZD | Sary Tauku, Kazakhstan | NOAA | F | 44.1° N | 76.8° E | 601 |
| LEF | Park Falls, Wisconsin | NOAA | F | 45.9° N | 90.3° W | 868 |
| LLN | Lulin, Taiwan | NOAA | F | 23.5° N | 120.9° E | 2867 |
| LUT | Lutjewad, Netherlands | RUG-CIO | C | 53.4° N | 6.4° E | 60 |
| MHD | Mace Head, Ireland | AGAGE | C | 53.3° N | 9.9° W | 25 |
| MLO | Mauna Loa, Hawaii | NOAA | F | 19.5° N | 155.6° W | 3397 |
| NWR | Niwot Ridge | NOAA | F | 40.0° N | 105.5° W | 3526 |
| NMB | Gobabeb, Namibia | NOAA | F | 23.6° S | 15.0° E | 456 |
| OXK | Ochsenkopf, Germany | MPI-BGC | C | 50.1° N | 11.8° E | 1185 |
| PAL | Pallas, Finland | FMI | C | 68.0° N | 24.1° W | 560 |
| PSA | Palmer Stn, Antarctica | NOAA | F | 64.9° S | 64.0° W | 10 |
| PTA | Point Arena, California | NOAA | F | 39.0° N | 123.7° W | 55 |
| RPB | Ragged Point, Barbados | AGAGE | C | 13.2° N | 59.4° W | 45 |
| SEY | Mahé, Seychelles | NOAA | F | 4.7° S | 55.2° E | 3 |
| SHM | Shemya Isl., Alaska | NOAA | F | 52.7° N | 174.1° E | 40 |
| SIS | Shetland Isl., UK | MPI-BGC | F | 59.9° N | 1.3° W | 46 |
| SSL | Schauinsland | UBA | C | 47.9° N | 7.9° E | 1205 |
| SMO | Tutuila, American Samoa | AGAGE | C | 14.3° S | 170.6° W | 42 |
| SPO | South Pole, Antarctica | NOAA | F | 89.98° S | 24.8° W | 2810 |
| STM | ocean stn. M, Norway | NOAA | F | 66.0° N | 2.0° E | 7 |
| SUM | Summit, Greenland | NOAA | F | 72.6° N | 38.5° W | 3238 |
| SYO | Syowa Stn., Antarctica | NOAA | F | 69.0° S | 39.6° E | 11 |
| TAP | Tae-ahn Peninsula, Taiwan | NOAA | F | 36.7° N | 126.1° E | 20 |
| TDF | Tierra del Fuego, Argentina | NOAA | F | 54.9° S | 68.5° W | 20 |
| THD | Trinidad Head, California | AGAGE | C | 41.1° N | 124.2° W | 107 |
| TTA | Griffin, UK | UEDIN | C | 56.6° N | 3.0° W | 535 |
| UTA | Wendover, Utah | NOAA | F | 39.9° N | 113.7° W | 132 |

Table 4. Continued.

| ID | Station | Operator | Type | Latitude | Longitude | Altitude (m a.s.l.) |
|-----|----------------------|----------|------|----------|-----------|---------------------|
| UUM | Ulaan-Uul, Mongolia | NOAA | F | 44.5° N | 111.1° E | 914 |
| WIS | Negev Desert, Israel | NOAA | F | 31.1° N | 34.9° E | 400 |
| WKT | Moody, Texas | NOAA | F | 31.3° N | 97.3° W | 708 |
| WLG | Mt. Waliguan, China | NOAA | F | 36.3° N | 100.9° E | 3810 |
| ZEP | Ny-Ålesund | NOAA | F | 78.9° N | 11.88° E | 475 |
| ZOT | Zotto, Russia | MPI-BGC | F | 60.8° N | 89.4° E | 415 |

Table 5. A priori and a posteriori calibration offsets (ppb) relative to the NOAA2006A scale. Note that only LMDZ4-I and TM5-I included the optimization of calibration offsets and only TM5 calculated these annually (the range over all years is given in brackets for TM5-I).

| ID | Prior | TM5-I | LMDZ4-I | ID | Prior | TM5-I | LMDZ4-I |
|-----|-------|-----------------------|---------|---------|-------|-------------------|---------|
| BIK | 0.06 | 0.22 (0.00–0.47) | 0.13 | PAL | 0.50 | 0.00 (0.0–0.0) | 0.32 |
| CBW | 0.27 | 0.52 (0.25–0.76) | 0.84 | MHD | 0.25 | 0.08 (0.25–0.76) | 0.05 |
| HUN | 1.08 | 0.45 (0.24–0.59) | 0.44 | THD | −0.30 | 0.04 (−0.01–0.07) | 0.28 |
| LUT | −3.0 | −1.2 (−2.0–0.0) | −2.0 | RPB | 0.00 | −0.11 (−0.21–0.0) | 0.07 |
| OXK | 0.39 | 0.77 (0.0–1.28) | 1.13 | SMO | 0.20 | 0.24 (0.14–0.37) | 0.36 |
| TTA | 0.00 | 0.56 (0.0–1.03) | 0.65 | CGO | 0.20 | 0.08 (0.0–0.13) | 0.00 |
| JFJ | 0.00 | −0.47 (−0.69–0.34) | −0.60 | NIES | −0.60 | 0.00 (0.0–0.0) | −0.41 |
| SSL | 0.00 | 0.30 (0.07–0.50) | 0.17 | MPI-BGC | 0.00 | 0.38 (0.19–0.54) | 0.47 |

Figure 1. Map of surface sites for atmospheric N₂O observations.

on the same scale, there still may be offsets owing to systematic errors. These offsets can introduce significant errors in the optimized fluxes if they are not accounted for prior to, or in, the inversion. For this reason, calibration offsets were estimated using inter-calibration data for each of the in situ stations, and for the three MPI-BGC flask sites together, rela-

tive to the NOAA-2006A scale (see Table 5). Since the inter-calibration data were not complete for all times and all sites, the offsets were included into the optimization problem in inversion frameworks with this capacity (i.e. in LMDZ4-I and TM5-I, and only TM5-I resolves the offsets temporally using annual resolution). In this case, the best estimates of the offsets were used as prior values. In the case that they could not be optimized (i.e. in MOZART4-I, ACMTt42167-I, and TM3-I) the given values were used to correct the observations prior to the inversion.

3 Results and discussion

3.1 Validation with atmospheric observations

3.1.1 Meridional gradients

Meridional gradients are some of the most commonly used observational parameters to assess CTMs, as they provide a constraint on features such as inter-hemispheric transport and latitudinal flux distributions (Gloor et al., 2007; Patra et al., 2011). Figure 2 shows the observed annual mean meridional mole fractions (2006 to 2009) compared with simulations

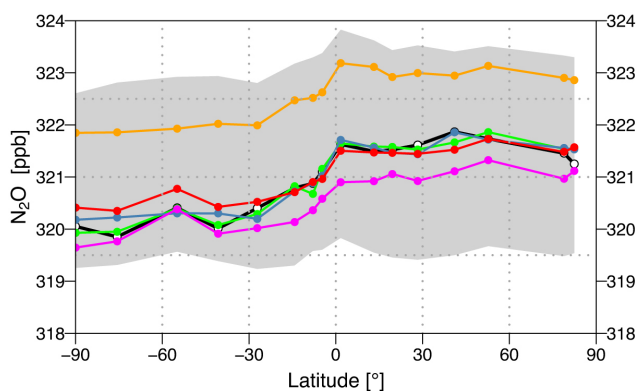


Figure 2. Comparison of the annual mean meridional N₂O mole fraction (ppb) from the posterior simulations with that from surface observations (average 2006–2009). The grey shaded area shows the range of values for all models using the prior fluxes. (Legend: observations, black; MOZART4-I, orange; ACTMt42l67-I, green; TM5-I, blue; TM3-I, red; LMDZ4-I, magenta).

by each CTM integrated with the corresponding posterior fluxes. For both the observations and the simulations, the gradients were calculated from detrended and deseasonalized N₂O mole fractions at background surface sites. For each model, a very good agreement was found with the gradient derived from surface observations (correlation coefficient $R^2 \geq 0.9$ for each model). In MOZART4-I, the mean mole fraction is approximately 1.5 ppb higher, which is most likely due to too high mole fractions in the initial conditions (see also Fig. S1 in the Supplement), but it still captures the gradient reasonably well.

Gradients in the pressure-weighted column mean N₂O were also compared against observations from HIPPO (Hi-per Pole-to-Pole Observations, <http://hippo.ucar.edu>) campaigns in January and November 2009 (Fig. 3). In contrast to the surface, the simulations all underestimate the total column inter-hemispheric gradient in January by about 1 ppb (circa 50 %). In November, the inter-hemispheric gradient is smaller and is matched more closely by the models; however, there is an overall offset of about 1 ppb (except MOZART4-I where its 1.5 ppb offset compensates). The offset in November may be in part due to a calibration difference between HIPPO and the NOAA data, which were used in the inversion, as comparisons of the HIPPO data between 0 and 2000 m around 19° N and 14° S with the NOAA data at Mauna Loa (19.5° N, 155.6° W) and Samoa (14.3° S, 170.6° E), respectively, show an offset of about 0.5 ppb. The underestimate of the gradient in January may be due to the models underestimating N₂O mole fractions in the upper troposphere as the agreement with the observed column is much better up to 2000 m, within a few tenths of a ppb (except north of about 50° N) (Fig. S2 in the Supplement). Kort et al. (2011) obtained a similar result when they assimilated only surface data (i.e. within 250–750 m above sea level)

from the HIPPO campaigns, finding that the simulations using the optimized fluxes underestimated the column mean N₂O but if the total column was assimilated, larger tropical fluxes were obtained and the total column matched the observations. Kort et al. (2011) reasoned that this was because the surface network failed to detect high N₂O signals in the tropics and that these were lofted to higher altitudes with strong tropical convection. If the fluxes in this study were underestimated for this reason, then this would result in a too low growth rate of N₂O in the troposphere. However, all models capture the observed growth rate within 0.17 ppb yr⁻¹ (20 %) and most within 0.1 ppb yr⁻¹ (10 %) (Fig. S3). The simulated upper troposphere values of N₂O in January may also be underestimated due to model transport errors such as too strong STE as was suggested in Part 1 of the inter-comparison (Thompson et al., 2014b), which would be much more apparent in the mole fractions above the planetary boundary layer (PBL) and is consistent with what we find in the comparisons up to 2000 m versus up to 10 000 m. If this were the case, and if no bias correction were applied to account for the transport error, then assimilating observations in the upper troposphere may lead to a systematic overestimate of the emissions.

3.1.2 Seasonal cycles

In Part 1 of the inter-comparison, considerable attention was paid to the seasonal cycle of N₂O as this is sensitive to STE, the height of the PBL, inter-hemispheric mixing, and seasonality in the fluxes. Figure 4 shows the annual mean (2006 to 2009) seasonal cycles from the posterior model simulations and observations at six key background sites. In the NH mid- to high latitudes, i.e. at MHD and BRW, the phase and amplitude are reasonably well captured by ACTMt42l67-I, TM5-I and LMDZ4-I with a minimum occurring in August, whereas MOZART4-I and TM3-I simulate a too early minimum at both sites by up to 2.5 months, as was also the case for all CTMs a priori. However, all five CTMs participating in Part 2 were able to capture the correct phase when using an alternative prior flux estimate with no terrestrial biosphere seasonal cycle (see Part 1, Thompson et al., 2014b) suggesting that the reason for the too early minimum was not related to transport problems but rather to the seasonality in the fluxes. This also seems to be the case for MOZART4-I and TM3-I, which have the smallest shift in the seasonal cycle relative to the prior fluxes (this is discussed in more detail in Sect. 3.2.3). At MLO, all CTMs simulate a too early minimum as was also the case using the a priori emissions. However, with the a posteriori emissions, the amplitude is closer to that observed. The timing of the minimum, in April, in the models is consistent with the expected maximum influence of stratospheric air in the troposphere owing to the downward branch of the Brewer–Dobson circulation, which has a maximum in December to February in the NH. However, the fact that the observed minimum occurs later may suggest that

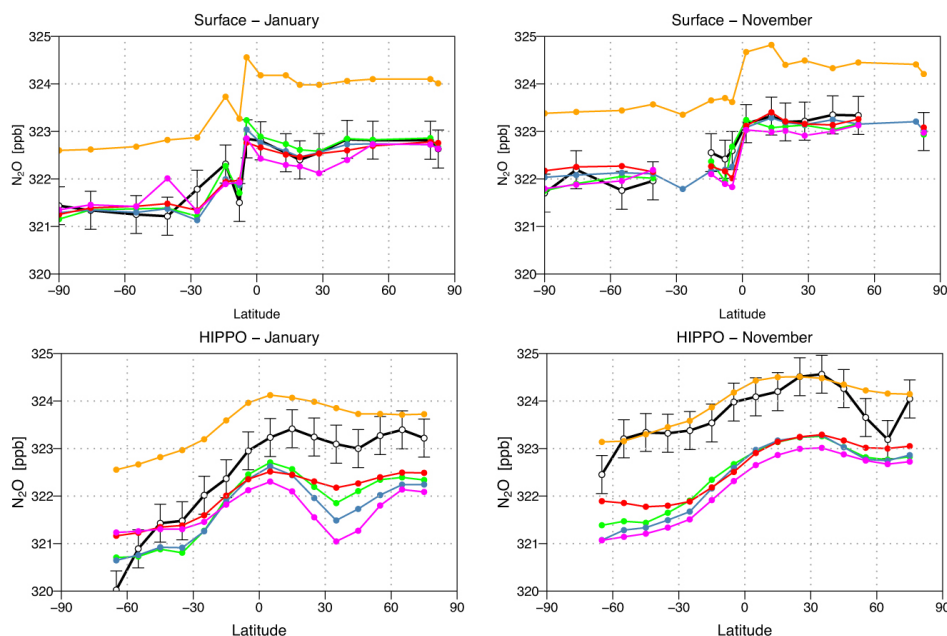


Figure 3. Comparison of model simulations (using the posterior fluxes) with observations of N₂O mole fraction (ppb) from surface sites (top row) and pressure-weighted column averages (up to 10 000 m) from HIPPO aircraft profiles (bottom row) for January (left) and November (right) 2009. (Legend: observations, black; MOZART4-I, orange; ACTMt42167-I, green; TM5-I, blue; TM3-I, red; LMDZ4-I, magenta).

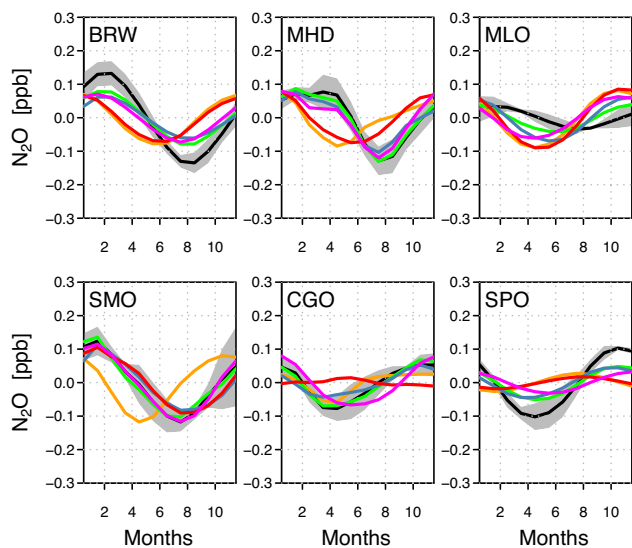


Figure 4. Comparison of the mean (2006–2008) observed and simulated seasonal cycles (using the posterior fluxes) in N₂O mole fraction (ppb) at selected key sites. The grey shading indicates the range of uncertainty (1 σ standard deviation) in the observations. For a description of the site abbreviations see Table 4. (Legend: observations, black; MOZART4-I, orange; ACTMt42167-I, green; TM5-I, blue; TM3-I, red; LMDZ4-I, magenta).

the influence of stratosphere to troposphere transport (STT) is overestimated in the models and/or that the seasonality is still not correct in the fluxes at the latitude of MLO.

For the Southern Hemisphere sites, SMO and CGO, all models agree well with the observed seasonal cycles except MOZART4-I at SMO and TM3-I at CGO. At SPO, however, all models underestimate the amplitude and MOZART4-I and TM3-I are also out of phase. It has been shown with N₂O isotope measurements that the seasonality at CGO is determined by the combined influences of STT and ocean fluxes leading to the observed minimum in April (Park et al., 2012). With the a priori fluxes, both TM3-I and LMDZ4-I had the phase of the seasonal cycle at CGO out by nearly 6 months indicating a problem with STT in the Southern Hemisphere (see Thompson et al., 2014b). A similar error in MOZART4-I was observed at SPO as well. However, a posteriori, LMDZ4-I has a much-improved fit to the phase at CGO and SPO, which was achieved by increasing the amplitude of the flux seasonality in the Southern Ocean, whereas TM3-I and MOZART4-I make nearly no adjustment (this is discussed further in Sect. 3.2.3).

3.2 Comparison of posterior emissions

In this section, we present a comparison of the posterior emission estimates. All posterior emissions were compared after they were interpolated from the corresponding model grid to 1° × 1° resolution.

Table 6. Overview of the prior and posterior global annual total source (upper panel) and sink (lower panel) (both in TgN yr⁻¹).

| Year | Prior | MOZART4-I | ACTMt42l67-I | TM5-I | TM3-I | LMDZ4-I |
|------|-------|-----------|--------------|-------|-------|---------|
| 2006 | 16.3 | 14.1 | 16.0 | 16.9 | 15.1 | 17.6 |
| 2007 | 16.8 | 15.6 | 16.7 | 16.9 | 16.6 | 19.1 |
| 2008 | 16.2 | 15.7 | 16.5 | 17.2 | 16.4 | 19.4 |
| 2009 | 16.4 | 14.4 | 15.5 | 15.4 | 15.6 | 18.8 |
| 2006 | – | 12.8 | 11.9 | 12.2 | 12.4 | 12.7 |
| 2007 | – | 12.6 | 12.4 | 12.6 | 12.4 | 12.7 |
| 2008 | – | 12.6 | 12.5 | 12.4 | 12.5 | 12.5 |
| 2009 | – | 12.7 | 13.0 | 12.4 | 12.6 | 12.7 |

3.2.1 Global means

Table 6 shows the global total emission a priori and the global total emission and sink a posteriori calculated by each inversion framework. On the basis of the posterior emissions, the inversions can be grouped into two categories: (1) those with low global totals, i.e. MOZART4-I, ACTMt42l67-I and TM3-I and (2) those with high global totals, i.e. TM5-I and LMDZ4-I, where low and high are defined relative to the prior. In the case of MOZART4-I, the low global total (the lowest of all inversions) results from the overestimate of N₂O mole fractions in the initial conditions, which leads to the emissions being underestimated and a too low atmospheric N₂O growth rate (see Fig. S3 in the Supplement). For this reason, the MOZART4-I estimates are not included further in the flux totals. However, in general, the low/high categorization also corresponds to how the observations were assimilated in the inversion; the first category inversions assimilate monthly (MOZART4-I and ACTMt42l67-I) or weekly (TM3-I) means, while those in the second category (TM5-I and LMDZ4-I) use the afternoon means for sites within the PBL and night-time means for mountain sites. This feature of the category 2 inversions means that they are also sensitive to the synoptic variability of the observations, while in the category 1 inversions this signal is smoothed out. Furthermore, the category 1 inversions may overestimate the monthly/weekly mean N₂O mole fraction a priori as compared to the NOAA CCGG flask measurements, since the flask samples are generally collected during meteorological conditions corresponding to background air, whereas in the model, it is the monthly/weekly mean of all data. MOZART4-I and ACTMt42l67-I, which have the lowest global total estimates, also differ from the other inversions in that they solve for emissions in large regions as opposed to solving the emissions at the resolution of the transport model. All inversion frameworks had very similar global total sinks, within less than 1 TgN yr⁻¹ of each other for each year, thus differences in the calculated loss rate is not a reason for the differences in global total emissions.

Overall, the global distribution of N₂O emissions was similar in all inversions and close to that a priori (Fig. 5). The

highest emissions were found in the subtropical and tropical regions of South America, Africa and Asia, in Europe and the eastern states of the USA. However, the inversions differ in the relative importance of emissions in each of these sub-continental regions. Figure 6 shows the annual mean flux increments made by each inversion, i.e. the posterior minus prior annual mean flux. There are a number of features in the increments that are common to all inversions: (1) lower (relative to the prior) emissions in temperate land regions in the SH, (2) higher emissions in central Europe, (3) higher emissions in central Africa and (4) no significant change in northern Eurasia and Canada. On the other hand, the inversions differ significantly in the direction and/or magnitude of the flux increments for the USA (eastern states), South and East Asia, and tropical South America. This information is summarized in Fig. 7, which shows the median absolute deviation (MAD) of the annual mean emissions from all five inversions. Regions with highest MAD correspond to regions with the greatest discrepancy among the inversions.

To better examine the differences between the a posteriori emissions, we compare the annual mean zonally integrated emissions plotted against latitude and the accumulated emissions from south to north (Fig. 8). By plotting the emissions in this way, differences in the latitudinal distribution of the emissions are more apparent and may be assessed in terms of different features of the CTMs used in the inversions, such as the rate of inter-hemispheric and vertical mixing. Moving from south to north, one can see that all inversions estimate lower emissions compared to the prior in the Southern Hemisphere; it is only north of the Equator that some of the inversions have a higher accumulated emission. TM5-I has the highest emission estimate for the Southern Hemisphere tropics and is also the most southern crossing point with the prior accumulated emissions. This is likely related to the fact that TM5-I has a long inter-hemispheric exchange time (1.7 years compared to the observed 1.4 years in 2006, based on SF₆ mole fractions at BRW, MLO, CGO and SPO; Patra et al., 2011), which would mean that in order to match the observed atmospheric N₂O mole fraction in the Southern Hemisphere tropics, higher emissions in this region are required. It can be expected that TM5-I would also for this reason

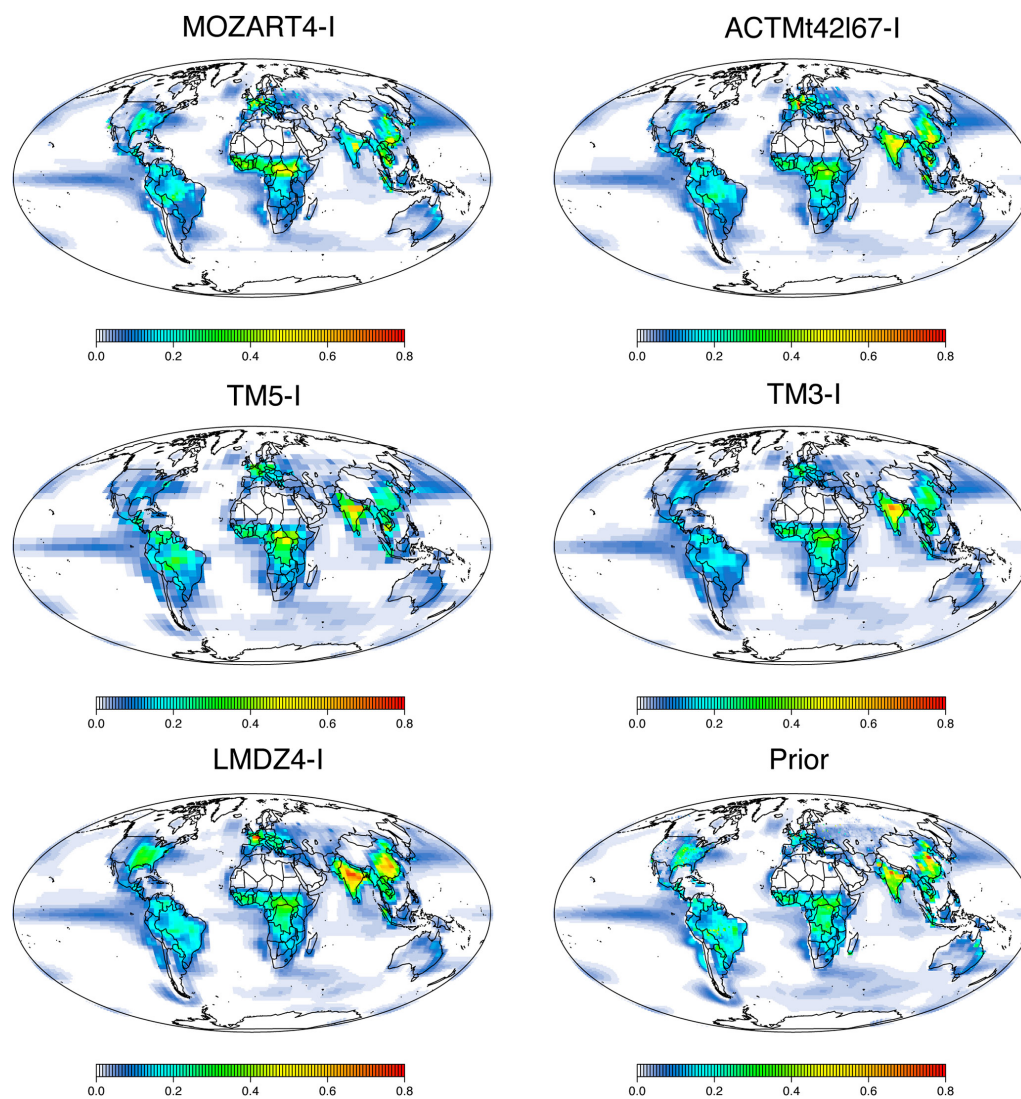


Figure 5. Maps of annual mean posterior and prior N₂O flux ($\text{gN m}^{-2} \text{yr}^{-1}$) for 2006–2008.

Table 7. Annual mean (2006–2008) regional N₂O emission estimates (TgN yr^{-1}). Values for which the inversions differ on the direction of the change with respect to the prior are shown in parentheses (MAD = median absolute deviation).

| Region | Prior | Posterior Range | Posterior Median | MAD | LMDZ4-I uncertainty |
|-------------------|-------|--------------------|---------------------|------|------------------------|
| Ocean 90–30° S | 1.49 | 0.92–1.34 | 1.08 | 0.20 | 0.39 |
| Ocean 30° S–30° N | 3.30 | 3.25–3.69 | (3.66) | 0.03 | 0.61 |
| Ocean 30–90° N | 0.95 | 1.13–1.29 | 1.20 | 0.08 | 0.32 |
| S + Tr America | 2.55 | 1.99–2.62 | (2.33) | 0.27 | 1.13 |
| N America | 1.00 | 0.65–1.29 | (0.74) | 0.11 | 0.28 |
| Africa | 3.07 | 3.23–3.40 | 3.36 | 0.04 | 0.70 |
| Europe | 0.80 | 0.84–1.20 | 1.04 | 0.20 | 0.19 |
| N Asia | 0.40 | 0.31–0.67 | (0.40) | 0.09 | 0.42 |
| S Asia | 2.91 | 2.56–3.81 | (2.85) | 0.28 | 0.77 |
| Australasia | 0.39 | 0.27–0.36 | 0.31 | 0.01 | 0.23 |

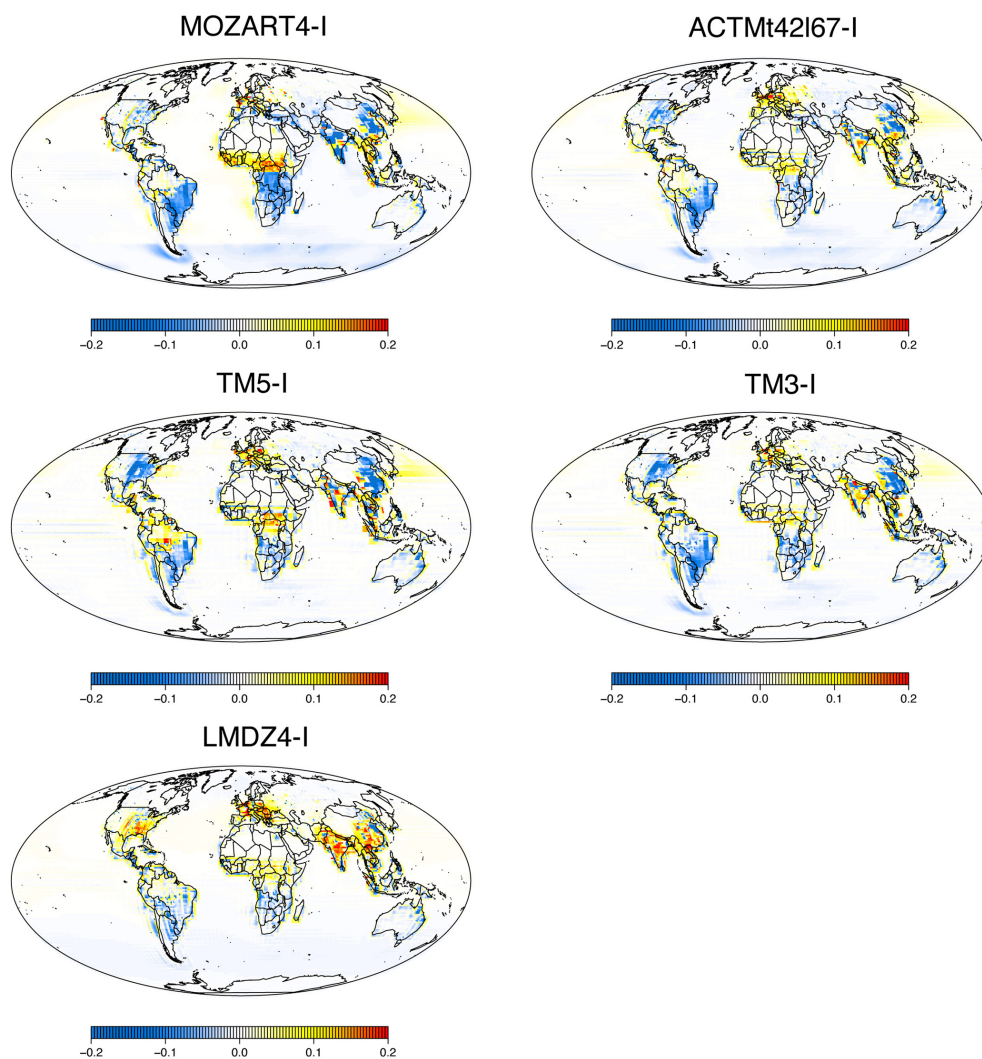


Figure 6. Maps of annual mean flux increments for 2006–2008 ($\text{gN m}^{-2} \text{yr}^{-1}$). Negative values (blue) indicate posterior fluxes that are lower than the prior fluxes and vice versa for positive ones (yellow-red).

estimate lower emissions in the Northern Hemisphere tropics and subtropics. However, the accumulated emissions still exceed those of e.g. LMDZ until circa 30°N . The reason for this cannot be determined from these results alone but it may be at least in part also owing to transport errors in LMDZ. At circa 30°N , LMDZ4-I surpasses both the prior and TM5-I accumulated emissions owing to very large emission estimates in the Northern Hemisphere subtropics. LMDZ4-I (in the present 19-layer configuration) has a relatively short inter-hemispheric exchange time, 1.2 years in 2006 (Patra et al., 2011), and has been found to have a very diffusive PBL in the Northern Hemisphere midlatitudes (Geels et al., 2007). These features likely lead to too high emissions in the northern subtropics and midlatitudes. North of circa 50°N , the zonally integrated emission differs very little among the inversions and the prior, however, the accumulated total emission at 90°N differs owing to the aforementioned disparities.

3.2.2 Regional means

Figure 9 shows the annual mean total emissions for seven sub-continental and three ocean regions from each of the inversions and the prior, the corresponding range, median, and MAD of the emissions, as well as the uncertainty calculated from a single inversion model (LMDZ-I), are given in Table 7. The calculated uncertainties per region are larger than the corresponding MAD values, indicating that the spread of posterior emissions is smaller than the uncertainty calculated for a single inversion. For only three out of the seven land regions is there a significant change in emissions with respect to the prior. Here, we define significant to mean that: (1) all inversions agree on the direction of the change and (2) the prior value is outside the range of the posterior median and plus or minus MAD. These regions are Africa, Europe and Australasia. For Australasia, the contribution to the global

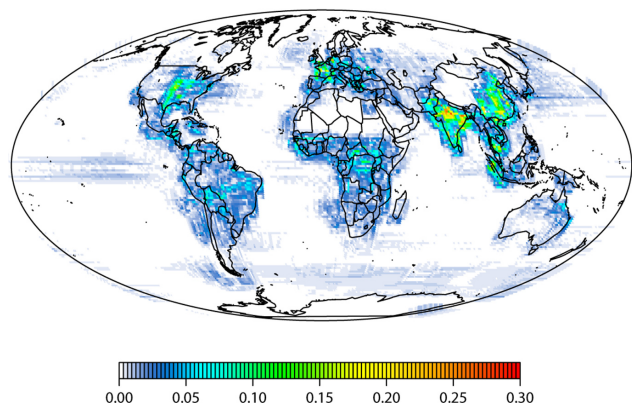


Figure 7. Map of median absolute deviation (MAD) of annual mean fluxes ($\text{gN m}^{-2} \text{yr}^{-1}$). The colour scale from white to red shows increasing MAD values.

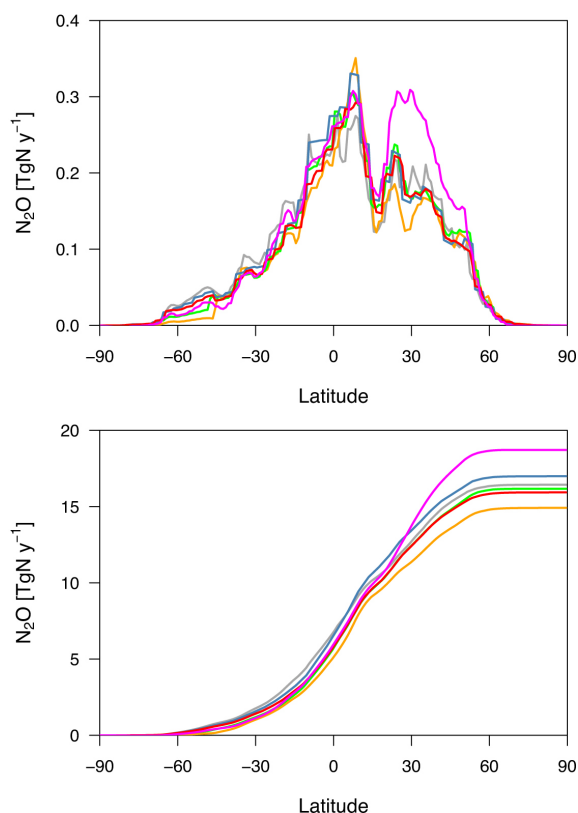


Figure 8. Zonally integrated annual mean (2006–2008) fluxes (top) and accumulated from south to north (bottom). (Legend: prior, grey; MOZART4-I, orange; ACTMT42I67-I, green; TM5-I, blue; TM3-I, red; LMDZ4-I, magenta).

total (2 %, median posterior value) and the absolute change relative to the prior (0.08 TgN yr^{-1}) are very small, and thus this region is not discussed further. Europe was found to have 30 % (0.24 TgN yr^{-1}) higher emissions than estimated a priori and contributes on average 6 % (median posterior value)

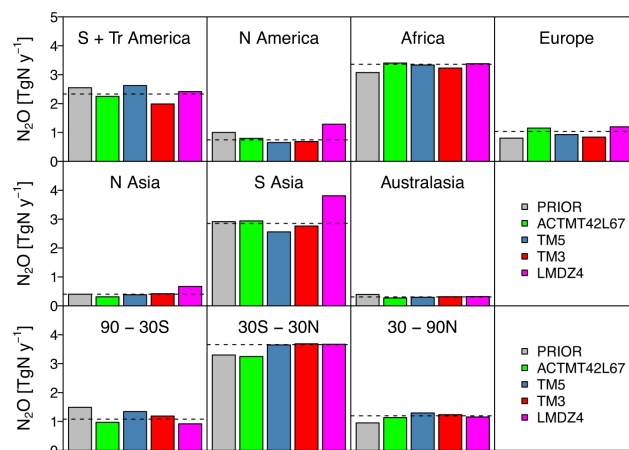


Figure 9. Annual mean (2006–2008) regional emission estimates (TgN yr^{-1}) for the seven land regions (first two rows) and three ocean regions (last row). The colours refer to the different inversion frameworks as indicated in the legend and the dashed line is the median of the posterior emissions.

to the global total emission. Africa was also found to have higher emissions relative to the prior (by 10 %, equivalent to 0.29 TgN yr^{-1}) and contributes 20 % to the global total emission. Of the regions where the change was not considered significant, North America as well as South and Tropical America still satisfied the second criterion. For North America, all inversions except LMDZ4-I estimated lower emissions (by 26 %, equivalent to 0.26 TgN yr^{-1}), bringing its contribution to the global total to 4 %, and for South and Tropical America, all inversions except TM5-I estimate lower emissions (by 9 %, equivalent to 0.22 TgN yr^{-1}) bringing its contribution to the global total to 14 %. For South Asia and North Asia, however, the inversions differed significantly both in the direction of change as well as in the magnitude. While the total emission from North Asia is small (2 % of the global), that from South Asia is very important (approximately 17 % of the global).

There are several reasons why the inversions differ so substantially for South Asia. First, this region is not well covered by the observation network. Emissions from this region are only constrained by the two in situ sites, HAT and COI, and by the discrete sampling sites, BKT, GMI, LLN, and TAP. Second, since the prior flux uncertainties are calculated proportionally to the prior flux, the prior uncertainty for this region is large allowing the inversions considerable freedom to adjust the fluxes here. Lastly, differences in the modelled transport, such as the tropical convection, monsoon flow, and shifts in the North Pacific storm track, which are important in determining outflow from the Asian continent (Stohl et al., 2002), may also contribute to the disparity among emission estimates for South Asia. Stohl et al. (2002) showed that tracers emitted in Asia south of 30° N , particularly in India, are readily transported toward the Intertropical Convergence

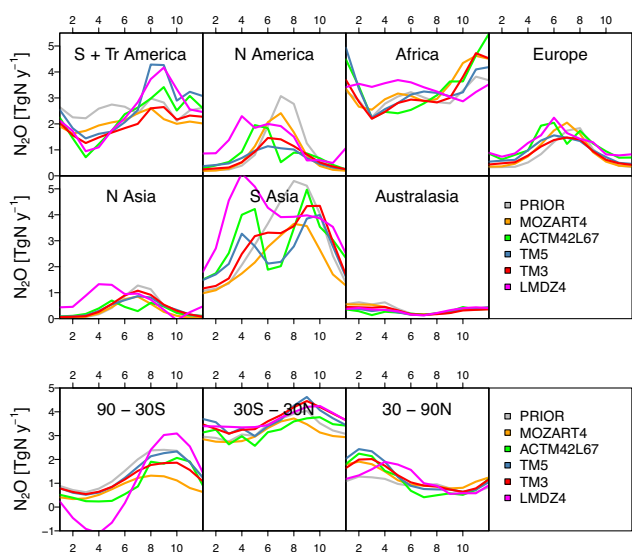


Figure 10. Mean (2006–2008) seasonal cycle in N₂O flux (TgN yr⁻¹) for each of the seven sub-continental regions (first two rows) and three ocean regions (last row).

Zone and thus could be one reason why LMDZ4-I, with a fast inter-hemispheric mixing rate, predicts the highest emissions for South Asia. Similar reasoning also applies to the large discrepancy for South and Tropical America. South and Tropical America is very poorly covered by the observation network (see Fig. 1) and the prior flux uncertainty for this region is very large. The posterior emission estimates for this region are also likely to be sensitive to features of the modelled transport, in particular, convective transport.

Unlike for the land regions, there is reasonably good agreement among the inversions for the ocean regions. All ocean regions satisfy the second criterion (i.e. the prior value is outside the range of the posterior median and MAD), and only the region 30° S–30° N does not also satisfy the first criterion (i.e. that all inversions agree on the direction of the change). The emissions for the Southern Ocean (90–30° S) were found to be smaller than estimated a priori, contributing 6 % (median posterior value) to the global total, while for the tropical (30° S–30° N) and northern (30–90° N) ocean regions, the emissions were found to be larger, contributing 22 % and 7 % to the global total, respectively.

3.2.3 Seasonal variability

The mean seasonal cycle for each of the seven land and three ocean regions was calculated by averaging the total monthly emissions over the period 2006 to 2008 and is shown in Fig. 10. For the Northern Hemisphere temperate land regions, Europe, North America and North Asia, the prior flux seasonal cycle predicts a late summer maximum, i.e. between July and August. However, all inversions estimate smaller emissions in July and/or August relative to the

prior. ACTMt42l67-I and LMDZ4-I both estimate an earlier and broader maximum, between April and June, while MOZART4-I, TM5-I and TM3-I predict a broader maximum between June and July. In Part 1 of the inter-comparison, it was shown in the CTM integrations using fluxes with a late summer maximum worsened the fit to the atmospheric observations compared to using fluxes with no seasonal cycle. The result for the Northern Hemisphere temperate regions in this study confirms the hypothesis in Part 1, that elevated emissions begin earlier in spring and continue until autumn without a peak in late summer. This is in line with what is expected based on the dependence of N₂O fluxes on soil moisture (measured by water-filled pore space, WFPS), soil temperature and the availability of nitrogen substrates, particularly NO₃⁻ and NH₄⁺ in soils (Butterbach-Bahl et al., 2013, and references therein). N₂O flux is maximized with WFPS of between approximately 70–90 % and has positive correlation with soil temperature (Smith et al., 1998). Therefore, low soil N₂O flux is expected throughout winter and higher N₂O is expected in summer so long as there is sufficient soil moisture and nitrogen substrate. N-fertilization usually occurs in spring and mid-summer providing sufficient nitrogen substrate, but drier soils in late summer may limit N₂O fluxes.

For the region of South Asia, there is some indication in the posterior fluxes of a double maximum, i.e. in ACTMt42l67-I, TM5-I and LMDZ4-I occurring in April and September. This approximately corresponds to the start and end of the Asian monsoon season, which lasts from April to September, while the period of lowest fluxes, from October to March, corresponds to the cool-dry season. This is in accordance with what has been found from in situ flux measurements in subtropical Southern China, which experiences annual monsoons – that is, that WFPS, soil NO₃⁻ and NH₄⁺ content, and N₂O fluxes were significantly higher in the hot-humid season than in the cool-dry season (Lin et al., 2010). However, the peak in spring may also partially be an artefact needed to compensate for the too low simulated spring atmospheric mole fraction as compared to the observations owing to a too strong influence of STT.

For the Southern Hemisphere regions of South and Tropical America and Africa, there is very little seasonality in the prior fluxes. However, all of the inversions estimate a March–April minimum for South and Tropical America and similarly (except LMDZ4-I) for Africa. For South and Tropical America, the March–April minimum is not easy to explain in terms of soil N₂O fluxes. In fact, from the few existing regional measurements of N₂O fluxes in tropical South America only a small seasonal cycle has been observed with elevated fluxes during the wet season from March–May (D’Amelio et al., 2009). Therefore, it is likely that the minimum in the optimized fluxes is due to transport errors since the timing of the atmospheric N₂O minimum in April, determined to a large extent by STT, is not captured by the models. Thus to match observations, the inversions estimate

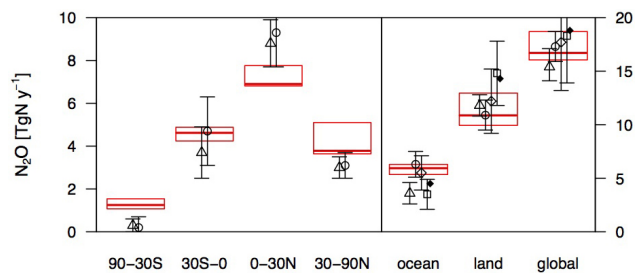


Figure 11. Comparison of the total emissions for each semi-hemisphere region, the ocean, land and globally from this study with previous estimates. The vertical extents of the red boxes indicate the range and the horizontal lines in the interior indicate the median of inversion estimates from this study. The points indicate the values from previous studies: Hirsch et al. (2006), open circles; Huang et al. (2008), triangles; AR4, diamonds; Syakila et al. (2011), solid circles; Zaehle et al. (2011), squares. The error bars indicate the 1σ uncertainty.

lower N₂O emissions at this time. It is possible that the impact of this transport error on the optimized fluxes would not be so strong if there were better observational constraints for South America. The same also applies for Africa where the minimum in March–April cannot be explained in terms of variability in soil fluxes as this time corresponds to the wet season when the highest N₂O emissions are expected.

For the ocean regions, the phase and amplitude of the seasonal cycles a posteriori differ little from those a priori. In the Southern Ocean, the minimum in April and maximum in September–October is consistent with the independent estimate of Nevison et al. (2005) and is largely driven by the upwelling and subsequent venting of subsurface water, which is enriched in N₂O. In LMDZ, however, the amplitude of the seasonal cycle is significantly larger, especially owing to the lower minimum in April, which is most likely also an artefact of the modelled transport. In the tropical and northern ocean regions, the seasonal cycle is much smaller in amplitude but is also likely driven by seasonal changes in upwelling.

3.3 Comparison with other estimates

To put this study into context with previous work, we compare our results to independent N₂O emission estimates. We have chosen five studies, including two atmospheric inversions (Hirsch et al., 2006; Huang et al., 2008) and three inventory and model-based estimates (Denman et al., 2007; Syakila and Kroeze, 2011; Zaehle et al., 2011), which are global in coverage and include estimates of N₂O emissions from all sources and are thus appropriate for this comparison. (The study of Zaehle et al. (2011) is not completely independent as it uses the same terrestrial biosphere model, O-CN, for the estimate of N₂O soil emissions as was used in this study's prior emissions; however, the O-CN simulations used different climate forcing and N-deposition.) Figure 11 com-

pare the global, land and ocean total emissions, as well as the emission distribution by semi-hemisphere, where available. Although the exact period of each study varies, they all include estimates of the global N₂O budget in the 2000s. At the global scale, all estimates agree within the range of uncertainties (no uncertainty estimate was provided by Syakila and Kroeze, 2011). Progress, however, has been made in reducing the level of uncertainty from 4.5 TgN yr⁻¹ in the IPCC AR4 (Intergovernmental Panel on Climate Change Fourth Assessment Report, 2007) to 0.7 TgN yr⁻¹ in this study (1σ , 68 % probability assuming Gaussian error distribution) with the complete range of inversions from 16.1 to 18.7 TgN yr⁻¹ for the mean 2006–2008. Previous studies differ in the apportionment between land and ocean emissions, with ocean estimates varying from 24 % to 38 % of the global total, whereas we found fairly good agreement among the inversions participating in this study with ocean estimates varying between 31 % and 38 % of the global total. At the semi-hemisphere scale, we find a few important differences between our median estimates and previous ones: for the region 90° S to 30° S we estimate higher emissions (7 % of the global total), for the region 0 to 30° N we estimate lower emissions (41 %), and for 30–90° N slightly higher emissions (23 %). Comparing the ratio for emissions in the regions 0–30° N and 30–90° N, all our inversions give a lower value (from 1.5 to 1.9) compared with 3.0 (Hirsch et al., 2006) and 2.9 (Huang et al., 2008) for the periods 1998–2005 and 2001–2005, respectively. Since our estimates are for a later period (2006–2008), this difference may reflect real changes in emissions. It is known that emissions have been increasing in Asia, particularly, in China, over the past decade, which has also increased the overall emission in the region 30–90° N, while no significant trends have been found in other regions (Thompson et al., 2014a). The increase in China has primarily been driven by an increase in N-fertilizer usage and to a lesser extent by an increase in industrial and combustion sources of N₂O (Thompson et al., 2014a).

4 Summary and conclusions

In this study we have compared the N₂O emission estimates of five inversion frameworks and analysed these in terms of their spatial distribution and seasonal variability. In general, there is a high level of agreement among the five inversions participating in this study despite the differences in inversion approach, atmospheric transport model and meteorological data used. This gives us confidence that there has been substantial progress made in terms of uncertainty reduction. Moreover, we have identified emission patterns that are robust – that is, common to all inversion frameworks – as well as those that depend strongly on the modelled transport and/or inversion set-up. The salient results are summarized as follows:

- the mean global annual N₂O emission ranges between 16.1 and 18.7 with a median and median absolute deviation (MAD) of 16.7 and 0.7 TgN yr⁻¹, respectively, for the years 2006 to 2008
- ocean emissions were found to contribute between 31 and 38 % and land emissions between 62 % and 69 % to the global total
- the apportionment of emissions to each semi-hemisphere was fairly close among inversions, with 7 ± 1 % to 90–30° S, 28 ± 2 % to 30° S–0°, 41 ± 1 % to 0–30° N and 23 ± 1 % to 30–90° N (median and MAD as a percentage of the global total), thus making the Northern Hemisphere tropics and subtropics the most important latitudinal range for N₂O emissions globally
- all inversions estimated lower emissions for the latitudes 90–30° S relative to the prior; however, the median estimate (7 % of the global total) was still higher than that found in previous studies (0 to 4 %)
- the ratio of emissions in 0–30° N to 30–90° N is smaller in all inversions (range of 1.52 to 1.91 and median of 1.9) compared to previous studies (2.9 and 3.0), representing a change in the percentage of the global total of –16 % for 0–30° N and of +3 % for 30–90° N
- all inversions estimated higher emissions in Europe and Africa relative to the prior, contributing 6 % (1.04 ± 0.20 TgN yr⁻¹) and 20 % (3.36 ± 0.04 TgN yr⁻¹) (median and MAD values) respectively to the global total compared with 5 % (0.80 TgN yr⁻¹) and 18 % (3.07 TgN yr⁻¹) a priori
- all inversions (except LMDZ4) estimate lower emissions in North America, contributing 4 % (0.74 ± 0.11 TgN yr⁻¹) (median values) to the global total compared to 6 % (1.00 TgN yr⁻¹) a priori
- all inversions (except TM5) estimate lower emissions in South and Tropical America, contributing 14 % (2.33 ± 0.27 TgN yr⁻¹) to the global total compared to 15 % (2.55 TgN yr⁻¹) a priori
- the largest uncertainties were found in the estimates for South and Tropical America and South Asia owing to uncertainties in the modelled atmospheric transport and to the poor observational constraint for these regions
- differences in the meridional distribution of emissions among the inversions were also found to depend on the inter-hemispheric mixing rate of the CTMs
- assimilating monthly mean observations from flask sampling networks most likely leads to an underestimate of the emissions

In general, the global N₂O budget, the total emissions and their spatial distribution, are close to what has been found from previous studies. One notable difference in our inversion estimates compared to previous ones though, is the shift in the distribution in the Northern Hemisphere, with lower emissions in the tropics and subtropics and higher emissions in temperate latitudes. Moreover, our inversions show a convergence of estimates both at the global and sub-continental scale. This good agreement is most likely due to the expansion of the atmospheric observation network. However, considerable uncertainties remain, especially in the less well-constrained regions of South Asia and South and Tropical America. These regions also appear to be very sensitive to uncertainties in the modelled atmospheric transport and are regions that should be targeted for new observation sites. Also sensitive to atmospheric transport, is the seasonal flux variability. Although this appears to be robust in the northern extratropics, for the tropics and southern extratropics, this is strongly dependent on having adequate representation of the timing of the maximum in stratosphere to troposphere transport (STT) and in vertical mixing, which is still not the case in most CTMs. However, inter-annual variations in fluxes are likely to be more robust as the year-to-year variations in STT are not as great as the seasonal variations. Improvements in the accuracy of N₂O emission estimates from atmospheric inversions, and a move towards emissions monitoring in the context of the Kyoto Protocol, would require improvements to modelling of atmospheric transport, in particular STT, which has a strong influence on tropospheric N₂O mole fractions.

The Supplement related to this article is available online at [doi:10.5194/acp-14-6177-2014-supplement](https://doi.org/10.5194/acp-14-6177-2014-supplement).

Acknowledgements. We would like to thank S. Zaehle, L. Bopp, and G. van der Werf for providing their N₂O emissions estimates. We also thank E. Kort and S. Wofsy for the use of the HIPPO data. Additionally, we would like to acknowledge everyone who contributes to the ongoing measurement of N₂O in all networks without which we would not have been able to make this inter-comparison study.

Edited by: W. Lahoz

References

- Butterbach-Bahl, K., Baggs, E. M., Dannenmann, M., Kiese, R., and Zechmeister-Boltenstern, S.: Nitrous oxide emissions from soils: how well do we understand the processes and their controls?, *Phil. Trans. Roy. Soc.*, 368, 1621, doi:10.1098/rstb.2013.0122, 2013.
- Butterbach-Bahl, K. and Dannenmann, M.: Denitrification and associated soil N₂O emissions due to agricultural activities in a changing climate, *Curr. Op. Environ. Sustain.*, 3, 389–395, 2011.
- Chevallier, F., Fisher, M., Peylin, P., Serrar, S., Bousquet, P., Bréon, F.-M., Chédin, A., and Ciais, P.: Inferring CO₂ sources and sinks from satellite observations: Method and application to TOVS data, *J. Geophys. Res.*, 110, D24309, doi:10.1029/2005JD006390, 2005.
- Corazza, M., Bergamaschi, P., Vermeulen, A. T., Aalto, T., Haszpra, L., Meinhardt, F., O'Doherty, S., Thompson, R., Moncrieff, J., Popa, E., Steinbacher, M., Jordan, A., Dlugokencky, E., Brühl, C., Krol, M. and Dentener, F.: Inverse modelling of European N₂O emissions: assimilating observations from different networks, *Atmos. Chem. Phys.*, 11, 2381–2398, doi:10.5194/acp-11-2381-2011, 2011.
- Courtier, P., Thépaut, J. N., and Hollingsworth, A.: A strategy for operational implementation of 4D-Var, using an incremental approach, *Q. J. Roy. Meteor. Soc.*, 120, 1367–1387, 1994.
- D'Amelio, M. T. S., Gatti, L. V., Miller, J. B., and Tans, P.: Regional N₂O fluxes in Amazonia derived from aircraft vertical profiles, *Atmos. Chem. Phys.*, 9, 8785–8797, doi:10.5194/acp-9-8785-2009, 2009.
- Denman, K. L., Brasseur, G. P., Chidthaisong, A., Ciais, P., Cox, P. M., Dickinson, R. E., Hauglustaine, D., Heinze, C., Holland, E., Jacob, D., Lohmann, U., Ramachandran, S., da Silva Dias, P. L., Wofsy, S. C. and Zhang, X.: Couplings Between Changes in the Climate System and Biogeochemistry, *Climate Change 2007: The Physical Science Basis. Contribution of Working Group I to the Fourth Assessment Report of the Intergovernmental Panel on Climate Change*, edited by: Solomon, S. D., Qin, D., Manning, M., Chen, Z., Marquis, M., Averyt, K. B., Tignor, M. and Miller, H. L., Cambridge University Press, Cambridge, 499–587, 2007.
- Duce, R. A., LaRoche, J., Altieri, K., Arrigo, K. R., Baker, A. R., Capone, D. G., Cornell, S., Dentener, F., Galloway, J., Ganeshram, R. S., Geider, R. J., Jickells, T., Kuypers, M. M., Langlois, R., Liss, P. S., Liu, S. M., Middelburg, J. J., Moore, C. M., Nickovic, S., Oschlies, A., Pedersen, T., Prospero, J., Schlitzer, R., Seitzinger, S., Sorensen, L. L., Uematsu, M., Ulloa, O., Voss, M., Ward, B., and Zamora, L.: Impacts of Atmospheric Anthropogenic Nitrogen on the Open Ocean, *Science*, 320, 893–897, 2008.
- Dutreuil, S., Bopp, L., and Tagliabue, A.: Impact of enhanced vertical mixing on marine biogeochemistry: lessons for geo-engineering and natural variability, *Biogeosciences*, 6, 901–912, doi:10.5194/bg-6-901-2009, 2009.
- Myhre, G., Shindell, D., Bréon, F.-M., Collins, W., Fuglesvedt, J., Huang, J., Koch, D., Lamarque, J.-F., Lee, D., Mendoza, B., Nakajima, T., Robock, A., Stephens, G., Takemura, T., and Zhang, H.: Anthropogenic and Natural Radiative Forcing, in: *Climate Change 2013: The Physical Science Basis Contribution of Working Group I to the Fifth Assessment Report of the Intergovernmental Panel on Climate Change*, edited by: Solomon, S., Qin, D., Manning, M., Chen, Z., Marquis, M., Averyt, K. B., Tignor, M., and Miller, H. L., Cambridge University Press. Cambridge, UK and New York, NY, USA, 2013.
- Galloway, J. N., Aber, J., Erisman, J. W., Seitzinger, S. P., Howarth, R. W., Cowling, E. B., and Cosby, B. J.: The Nitrogen Cascade, *Bioscience*, 53, 341–356, 2003.
- Geels, C., Gloor, M., Ciais, P., Bousquet, P., Peylin, P., Vermeulen, A. T., Dargaville, R., Aalto, T., Brandt, J., Christensen, J. H., Frohn, L. M., Haszpra, L., Karstens, U., Rödenbeck, C., Ramonet, M., Carboni, G., and Santaguida, R.: Comparing atmospheric transport models for future regional inversions over Europe – Part 1: mapping the atmospheric CO₂ signals, *Atmos. Chem. Phys.*, 7, 3461–3479, doi:10.5194/acp-7-3461-2007, 2007.
- Gloor, M., Dlugokencky, E., Brenninkmeijer, C., Horowitz, L., Hurst, D. F., Dutton, G., Crevoisier, C., Machida, T., and Tans, P.: Three-dimensional SF₆ data and tropospheric transport simulations: Signals, modeling accuracy, and implications for inverse modeling, *J. Geophys. Res.*, 112, D15112, doi:10.1029/2006jd007973, 2007.
- Hall, B. D., Dutton, G. S., and Elkins, J. W.: The NOAA nitrous oxide standard scale for atmospheric observations. *J. Geophys. Res.*, 112, D09305, doi:10.1029/2006JD007954, 2007.
- Hirsch, A. I., Michalak, A. M., Bruhwiler, L. M., Peters, W., Dlugokencky, E. J., and Tans, P. P.: Inverse modeling estimates of the global nitrous oxide surface flux from 1998–2001, *Global Biogeochem. Cy.*, 20, GB1008, doi:10.1029/2004GB002443, 2006.
- Huang, J., Golombek, A., Prinn, R., Weiss, R., Fraser, P., Simmonds, P., Dlugokencky, E. J., Hall, B., Elkins, J., Steele, P., Langenfelds, R., Krümmel, P., Dutton, P. and Porter, L.: Estimation of regional emissions of nitrous oxide from 1997 to 2005 using multinetwerk measurements, a chemical transport model, and an inverse method, *J. Geophys. Res.*, 113, D17313, doi:10.1029/2007JD009381, 2008.
- Kort, E. A., Patra, P. K., Ishijima, K., Daube, B. C., Jimenez, R., Elkins, J., Hurst, D., Moore, F. L., Sweeney, C. and Wofsy, S. C.: Tropospheric distribution and variability of N₂O: Evidence for strong tropical emissions, *Geophys. Res. Lett.*, 38, L15806, doi:10.1029/2011GL047612, 2011.
- Lin, S., Iqbal, J., Hu, R., and Feng, M.: N₂O emissions from different land uses in mid-subtropical China, *Agricult. Ecosyst. Environ.*, 136, 40–48, doi:10.1016/j.agee.2009.11.005, 2010.
- Minschwaner, K., Salawitch, R. J., and McElroy, M. B.: Absorption of Solar Radiation by O₂: Implications for O₃ and Lifetimes of N₂O, CFC₁₃, and CF₂Cl₂, *J. Geophys. Res.*, 98, 10543–10561, 1993.
- Nevison, C. D., Keeling, R. F., Weiss, R. F., Popp, B. N., Jin, X., Fraser, P. J., Porter, L. W., and Hess, P. G.: Southern Ocean ventilation inferred from seasonal cycles of atmospheric N₂O and O₂/N₂ at Cape Grim, Tasmania, *Tellus B*, 57, 218–229, 2005.
- Olivier, J. G. J., Van Aardenne, J. A., Dentener, F., Pagliari, V., Ganzeveld, L. N., and Peters, J. A. H. W.: Recent trends in global greenhouse gas emissions: regional trends 1970–2000 and spatial distribution of key sources in 2000, *Environ. Sci.*, 2, 81–99, doi:10.1080/15693430500400345, 2005.
- Park, S., Croteau, P., Boering, K. A., Etheridge, D. M., Ferretti, D., Fraser, P. J., Kim, K. R., Krümmel, P. B., Langenfelds, R. L., van Ommen, T. D., Steele, L. P., and Trudinger, C. M.: Trends and seasonal cycles in the isotopic composition of nitrous oxide since 1940, *Nature Geosci.*, 5, 261–265, 2012.

- Patra, P. K., Houweling, S., Krol, M., Bousquet, P., Belikov, D., Bergmann, D., Bian, H., Cameron-Smith, P., Chipperfield, M. P., Corbin, K., Fortems-Cheiney, A., Fraser, A., Gloor, E., Hess, P., Ito, A., Kawa, S. R., Law, R. M., Loh, Z., Maksyutov, S., Meng, L., Palmer, P. I., Prinn, R. G., Rigby, M., Saito, R., and Wilson, C.: TransCom model simulations of CH₄ and related species: linking transport, surface flux and chemical loss with CH₄ variability in the troposphere and lower stratosphere, *Atmos. Chem. Phys.*, 11, 12813–12837, doi:10.5194/acp-11-12813-2011, 2011.
- Prather, M. J., Holmes, C. D., and Hsu, J.: Reactive greenhouse gas scenarios: Systematic exploration of uncertainties and the role of atmospheric chemistry, *Geophys. Res. Lett.*, 39, L09803, doi:10.1029/2012GL051440, 2012.
- Prinn, R. G., Cunnold, D., Rasmussen, R., Simmonds, P., Alyea, F., Crawford, A., Fraser, P., and Rosen, R.: Atmospheric emissions and trends of nitrous oxide deduced from 10 years of ALE-GAGE data, *J. Geophys. Res.*, 95, 18369–18385, 1990.
- Prinn, R. G., Weiss, R. F., Fraser, P. J., Simmonds, P. G., Cunnold, D. M., Alyea, F. N., O'Doherty, S., Salameh, P., Miller, B. R., Huang, J., Wang, R. H. J., Hartley, D. E., Harth, C., Steele, L. P., Sturrock, G., Midgley, P. M., and McCulloch, A.: A history of chemically and radiatively important gases in air deduced from ALE/GAGE/AGAGE, *J. Geophys. Res.*, 105, 17751–17792, 2000.
- Ravishankara, A. R., Daniel, J. S., and Portmann, R. W.: Nitrous Oxide (N₂O): The Dominant Ozone-Depleting Substance Emitted in the 21st Century, *Science*, 326, 123–125, 2009.
- Rayner, P. J., Enting, I. G., Francey, R. J., and Langenfelds, R.: Reconstructing the recent carbon cycle from atmospheric CO₂, δ¹³C and O₂/N₂ observations, *Tellus B*, 51, 213–232, 1999.
- Rödenbeck, C.: Estimating CO₂ sources and sinks from atmospheric mixing ratio measurements using a global inversion of atmospheric transport. Technical Report. Jena, Max Planck Institute for Biogeochemistry, 6, 37 pp., 2005.
- Saikawa, E., Prinn, R. G., Dlugokencky, E., Ishijima, K., Dutton, G. S., Hall, B. D., Langenfelds, R., Tohjima, Y., Machida, T., Manizza, M., Rigby, M., O'Doherty, S., Patra, P. K., Harth, C. M., Weiss, R. F., Krümmel, P. B., van der Schoot, M., Fraser, P. J., Steele, L. P., Aoki, S., Nakazawa, T., and Elkins, J. W.: Global and regional emissions estimates for N₂O, *Atmos. Chem. Phys.*, 14, 4617–4641, doi:10.5194/acp-14-4617-2014, 2014.
- Smith, K. A., Thomson, P. E., Clayton, H., McTaggart, I. P., and Conen, F.: Effects of temperature, water content and nitrogen fertilisation on emissions of nitrous oxide by soils, *Atmos. Environ.*, 32, 3301–3309, 1998.
- Stohl, A., Eckhardt, S., Forster, C., James, P., and Spichtinger, N.: On the pathways and timescales of intercontinental air pollution transport, *J. Geophys. Res.-Atmos.*, 107, 4684, doi:10.1029/2001jd001396, 2002.
- Syakila, A. and Kroeze, C.: The global nitrous oxide budget revisited, *Greenhouse Gas Measurement and Management*, 1, 17–26, 2011.
- Tarantola, A.: Inverse problem theory and methods for model parameter estimation, Society for Industrial and Applied Mathematics, Philadelphia, 358 pp., 2005.
- Thompson, R. L., Bousquet, P., Chevallier, F., Rayner, P. J. and Ciais, P.: Impact of the atmospheric sink and vertical mixing on nitrous oxide fluxes estimated using inversion methods. *J. Geophys. Res.*, 116, D17307, doi:10.1029/2011JD015815, 2011a.
- Thompson, R. L., Gerbig, C., and Rödenbeck, C.: A Bayesian inversion estimate of N₂O emissions for western and central Europe and the assessment of aggregation errors, *Atmos. Chem. Phys.*, 11, 3443–3458, doi:10.5194/acp-11-3443-2011, 2011b.
- Thompson, R. L., Chevallier, F., Crotwell, A. M., Dutton, G., Langenfelds, R. L., Prinn, R. G., Weiss, R. F., Tohjima, Y., Nakazawa, T., Krümmel, P. B., Steele, L. P., Fraser, P., O'Doherty, S., Ishijima, K., and Aoki, S.: Nitrous oxide emissions 1999 to 2009 from a global atmospheric inversion, *Atmos. Chem. Phys.*, 14, 1801–1817, doi:10.5194/acp-14-1801-2014, 2014a.
- Thompson, R. L., Patra, P. K., Ishijima, K., Saikawa, E., Corazza, M., Karstens, U., Wilson, C., Bergamaschi, P., Dlugokencky, E., Sweeney, C., Prinn, R. G., Weiss, R. F., O'Doherty, S., Fraser, P. J., Steele, L. P., Krümmel, P. B., Saunio, M., Chipperfield, M., and Bousquet, P.: TransCom N₂O model inter-comparison – Part 1: Assessing the influence of transport and surface fluxes on tropospheric N₂O variability, *Atmos. Chem. Phys.*, 14, 4349–4368, doi:10.5194/acp-14-4349-2014, 2014b.
- van der Werf, G. R., Randerson, J. T., Giglio, L., Collatz, G. J., Mu, M., Kasibhatla, P. S., Morton, D. C., DeFries, R. S., Jin, Y., and van Leeuwen, T. T.: Global fire emissions and the contribution of deforestation, savanna, forest, agricultural, and peat fires (1997–2009), *Atmos. Chem. Phys.*, 10, 11707–11735, doi:10.5194/acp-10-11707-2010, 2010.
- Volk, C. M., Elkins, J. W., Fahey, D. W., Dutton, G. S., Gilligan, J. M., Loewenstein, M., Podolske, J. R., Chan, K. R., and Gunson, M. R.: Evaluation of source gas lifetimes from stratospheric observations, *J. Geophys. Res.*, 102, 25543–25564, 1997.
- Zaehle, S. and Friend, A. D.: Carbon and nitrogen cycle dynamics in the O-CN land surface model: 1. Model description, site-scale evaluation, and sensitivity to parameter estimates. *Global Biogeochem. Cy.*, 24, GB1005, doi:10.1029/2009Gb003521, 2010.
- Zaehle, S., Ciais, P., Friend, A. D., and Prieur, V.: Carbon benefits of anthropogenic reactive nitrogen offset by nitrous oxide emissions, *Nature Geosci.*, 4, 601–605, 2011.